

CANCER IMMUNOLOGY

Manipulating mitochondrial electron flow enhances tumor immunogenicity

Kailash Chandra Mangalhar^{1†}, Siva Karthik Varanasi^{1†}, Melissa A. Johnson¹, Mannix J. Burns¹, Gladys R. Rojas¹, Pau B. Esparza Molto¹, Alva G. Sainz^{1,2}, Nimesha Tadepalle¹, Keene L. Abbott^{3,4,5}, Gaurav Mendiratta^{1,†}, Dan Chen¹, Yagmur Farsakoglu¹, Tenzin Kunchok⁶, Filipe Araujo Hoffmann¹, Bianca Parisi¹, Mercedes Rincon⁷, Matthew G. Vander Heiden^{3,4,5}, Marcus Bosenberg⁸, Diana C. Hargreaves¹, Susan M. Kaech^{1*}, Gerald S. Shadel^{1*}

Although tumor growth requires the mitochondrial electron transport chain (ETC), the relative contribution of complex I (CI) and complex II (CII), the gatekeepers for initiating electron flow, remains unclear. In this work, we report that the loss of CII, but not that of CI, reduces melanoma tumor growth by increasing antigen presentation and T cell-mediated killing. This is driven by succinate-mediated transcriptional and epigenetic activation of major histocompatibility complex-antigen processing and presentation (MHC-APP) genes independent of interferon signaling. Furthermore, knockout of methylation-controlled J protein (MCJ), to promote electron entry preferentially through CI, provides proof of concept of ETC rewiring to achieve antitumor responses without side effects associated with an overall reduction in mitochondrial respiration in noncancer cells. Our results may hold therapeutic potential for tumors that have reduced MHC-APP expression, a common mechanism of cancer immune evasion.

The mitochondrial tricarboxylic acid (TCA) cycle and electron transport chain (ETC) provide metabolic plasticity required for cancer growth and progression (1, 2). The ETC comprises four multisubunit complexes: complexes I to IV (CI to CIV). CI [reduced form of NAD⁺ (NADH) dehydrogenase] and CII [succinate dehydrogenase (SDH)] are the gatekeepers of electron flow by passing electrons from TCA-generated NADH and flavin adenine dinucleotide (FADH₂), respectively, to ubiquinone for delivery to CIII and finally to oxygen via CIV. Recycling of ubiquinone by CIII is required for continuous flow of electrons through the ETC initiated by CI or CII and is essential for tumor growth (3–5). However, individual loss-of-function mutations in CI or CII subunits are tolerated in cancer cells through metabolic adaptations that are incompletely understood (6–13). Thus, in this work, we endeavored to learn more about the individual contributions of CI and CII activity to tumor growth, metabolism, and immunogenicity.

Reducing mitochondrial CII activity enhances antitumor immune responses

To investigate the contributions of CI and CII to tumor growth and antitumor immune responses, we generated isogenic CI (sg*Ndufa1*) or CII (sg*Sdhb* or sg*Sdhc*) knockout YUMM1.7 (Braf^{V600E}/Pten^{-/-}/Cdkn2a^{-/-}) mouse melanoma cells (14) (fig. S1A) and implanted them into immune-competent mice. Knockout of CI or CII subunits reduced the respective complexes as expected but did not affect the abundance of other ETC complexes (fig. S1B). Loss of CI or CII also significantly reduced oxygen consumption, spare respiratory capacity, and cell proliferation (fig. S1, C to E). However, CI knockout cells had lower respiration and proliferation compared with CII knockout cells, consistent with CI being the major source of electrons to the ETC in YUMM1.7 cells under these culture growth conditions. Knockout of CI increased NADH levels without affecting the CII substrate succinate, which suggests that CI knockout cells have intact CII-dependent respiration and succinate dehydrogenase activity (fig. S1, F and G). Conversely, knockout of CII increased succinate without affecting NADH levels, indicating that CI respiration is intact in CII knockout cells (fig. S1, F and G) but that CII-dependent respiration and succinate dehydrogenase activity are absent. We next engrafted CI or CII knockout cells into syngeneic, wild-type C57BL/6 mice. Unexpectedly, CI and CII knockout had notably differential effects on tumor growth. Despite proliferating slower in vitro compared with CII knockout (sg*Sdhb*) and control (sgSCR) cells, CI knockout (sg*Ndufa1*) tumors did not show any growth defects in vivo, which suggests that CI is not required for YUMM1.7 tumor growth (Fig. 1, A and B). However, CII knockout tumors grew significantly slower

compared with control and CI knockout tumors. Flow cytometry analysis of CII knockout tumors showed significantly increased immune cell (CD45⁺) infiltration, especially CD8⁺ T cells, relative to control and CI knockout tumors (Fig. 1, C and D). No significant change in the number of CD4⁺ T cells or the percentage of regulatory T cells (T_{regs}) was observed (fig. S2, A and B). Consistent with this, CD8⁺ T cells from CII knockout tumors produced more interferon-γ (IFN-γ⁺) and granzyme-B (GZMB⁺), which suggests that significant tumor-killing effector function was responsible for the observed antitumor activity (Fig. 1E). This was further confirmed by performing the same experiment in *Rag1*-deficient mice that do not have mature T cells or B cells, in which the antitumor phenotype of CII knockout was lost (fig. S2, C and D). Because antigen presentation by major histocompatibility complex class I (MHC-I) is a major determinant of T cell activation and killing, we next measured MHC-I expression on CI- and CII-deficient tumor cells. We found significantly higher MHC-I expression on CII knockout tumor cells compared with CI knockout and control tumor cells in vivo (Fig. 1F). Furthermore, ablation of antigen presentation by knocking out β2-microglobulin (MHC-I light chain, sg*B2m*) in CII knockout cells confirmed that tumor antigen presentation is required for the antitumor effect of CII depletion (Fig. 1, G and H, and fig. S2E). Consistent with these data, CIBERSORT correlation analysis of pan-cancer datasets showed a negative correlation between the expression of CII genes (*SDHA*, *SDHB*, *SDHC*, and *SDHD*) and a cytotoxic T cell gene signature across multiple cancer types (33/36 cancer types) (fig. S3A). Finally, low *SDHC* (CII subunit) expressing human breast and skin tumors also showed increased expression of cytotoxic T lymphocyte (CTL) marker genes (*CD8A*, *CD8B*, *GZMA*, *GZMB*, *IFNG*, and *PFR1*) (fig. S3, B and C, and table S1). Thus, we conclude that the loss of CII, but not of CI, results in a strong antitumor T cell response through increased antigen presentation.

Seemingly contrary to our findings, loss of CII function (i.e., SDHx subunit gene mutations) can be tumorigenic in humans, and succinate, which accumulates under these conditions, has been coined an “oncometabolite” (15, 16). Most of the oncogenic SDHx mutations are germline and result in a subset of rare cancers, such as pheochromocytoma, paraganglioma, and gastrointestinal stromal tumors (15). Thus, in these cases, CII deficiency and succinate accumulation would be present from the beginning and could promote early events in tumor initiation. Our results, by contrast, show that the depletion of CII reduces tumor growth by enhancing antigen presentation; thus, the effect is not on tumor initiation but rather on tumor growth resulting from immune system attack. It is also important to note that the loss of CII in mouse

¹Salk Institute for Biological Studies, La Jolla, CA 92037, USA.

²Department of Pathology, Yale University School of Medicine, New Haven, CT 06520, USA. ³Koch Institute for Integrative

Cancer Research, Massachusetts Institute of Technology, Cambridge, MA 02139, USA. ⁴Department of Biology, Massachusetts Institute of Technology, Cambridge, MA 02139, USA. ⁵Broad Institute of MIT and Harvard, Cambridge, MA 02142, USA. ⁶Whitehead Institute Metabolomics Core Facility, Cambridge, MA 02139, USA. ⁷Department of Immunology and Microbiology, University of Colorado Denver, Anschutz Medical Campus, Aurora, CO 80045, USA. ⁸Departments of Pathology, Dermatology, and Immunology, Yale University School of Medicine, New Haven, CT 06520, USA.

*Corresponding author. Email: skaech@salk.edu (S.M.K.); gshadel@salk.edu (G.S.S.)

†These authors contributed equally to this work.

‡Present address: Takeda Development Center America, San Diego, CA 92121, USA.

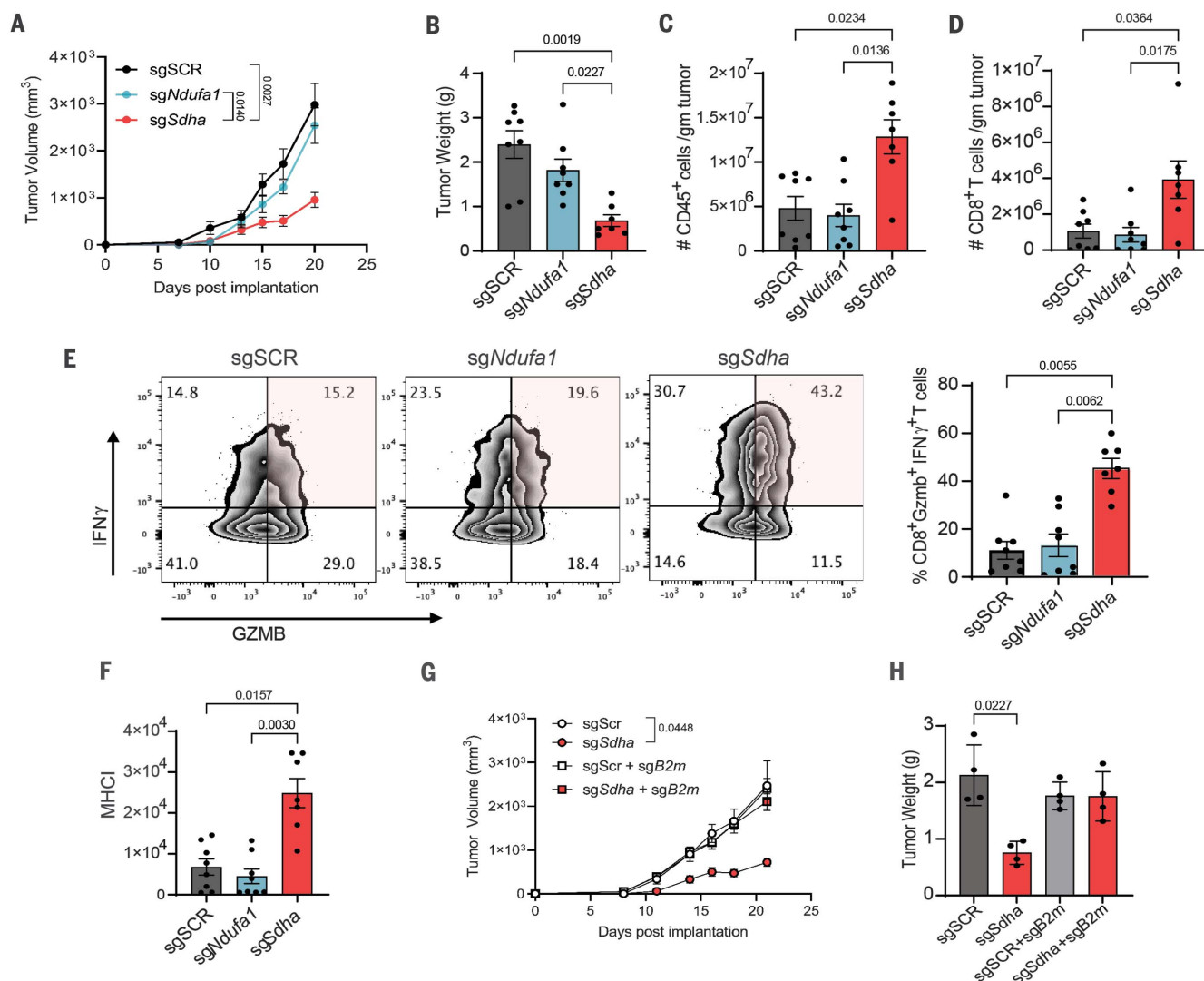


Fig. 1. Mitochondrial CII inhibition enhances antitumor immunity through increased MHC-I. YUMM1.7-sgSCR (control) ($n = 8$), sgSdha (CII knockout) ($n = 8$), and sgNdufa1 (CI knockout) ($n = 7$) cells (2×10^5) were subcutaneously injected into the flanks of C57BL/6 male mice, and tumor growth was monitored for 20 days. (A to D) Tumor growth curves: tumor volume versus time (days postimplantation) (A), tumor weight (in grams at day 20) (B), number of tumor-infiltrating CD45⁺ cells per gram of tumor at day 20 (C), and CD8⁺ T cells per gram of tumor at day 20 (D). (E) Percentage of IFN- γ ⁺ and GZMB⁺ positive tumor-infiltrating CD8⁺ T cells in tumors at day 20. (F) Tumor surface MHC-I

expression on cells from (A) at day 20. (G and H) Tumor growth curve (tumor volume versus time is plotted) (G) and tumor weight (in grams at day 21) (H) of tumors from sgSCR (control), sgSdha (CII knockout), sgSCR-sgB2m (control + $\beta 2$ microglobulin knockout), and sgSdha-sgB2m (CII knockout + $\beta 2$ microglobulin knockout) YUMM1.7 cells (2×10^5) subcutaneously implanted in C57BL/6 mice ($n = 4$). Data points in each panel represent independent samples from two experiments. Data are plotted as means \pm SEMs. Statistical significance was determined by Kruskal-Wallis test with Dunn's multiple comparisons test for (A) to (H).

models does not cause spontaneous tumor formation unless other oncogenic conditions are present (17–21). Additionally, inherited oncogenic CII mutations usually affect neuroendocrine tissues within specialized physiological environments and/or can promote specific tumor microenvironments that are conditionally tumorigenic when CII activity is inhibited and/or in combination with other oncogenic genetic alterations (18, 22–24). Finally, it is possible that the immune pressure we have uncovered that results from CII deficiency leads to immunoediting, promoting the selection of tumor clones with immunosuppressive prop-

erties that escape immune detection and continue to grow.

Mitochondrial succinate increases tumor antigen presentation independently of IFN signaling

Next, to better understand the antitumor response to CII deficiency, we explored the nature of the signal underlying the increased tumor cell antigen presentation. We first determined that depletion of CII increased cell surface expression of MHC-I in YUMM1.7 cells in vitro (Fig. 2A). Notably, pharmacological inhibition of CII by 3-nitropropionic acid (3-NPA), but not CI inhibition by rotenone, was suf-

ficient to increase MHC-I expression in vitro in multiple murine cell lines (YUMM1.7, 4T1, B16-F10, YUMMER, MC38, and fibroblasts; Fig. 2B and fig. S4, A and B). Inhibition of CII, but not of CI, increased the transcripts of several major histocompatibility complex–antigen processing and presentation (MHC-APP) genes in YUMM1.7 cells (Fig. 2C and fig. S4C). Similar results were obtained with 3-NPA-treated 4T1 mouse breast cancer cells (fig. S4D). Consistent with this, inhibition of CII in YUMM1.7 cells expressing ovalbumin (OVA), a model antigen, increased the presentation of the OVA-derived peptide SIINFEKL bound to MHC-I (H-2K^b),

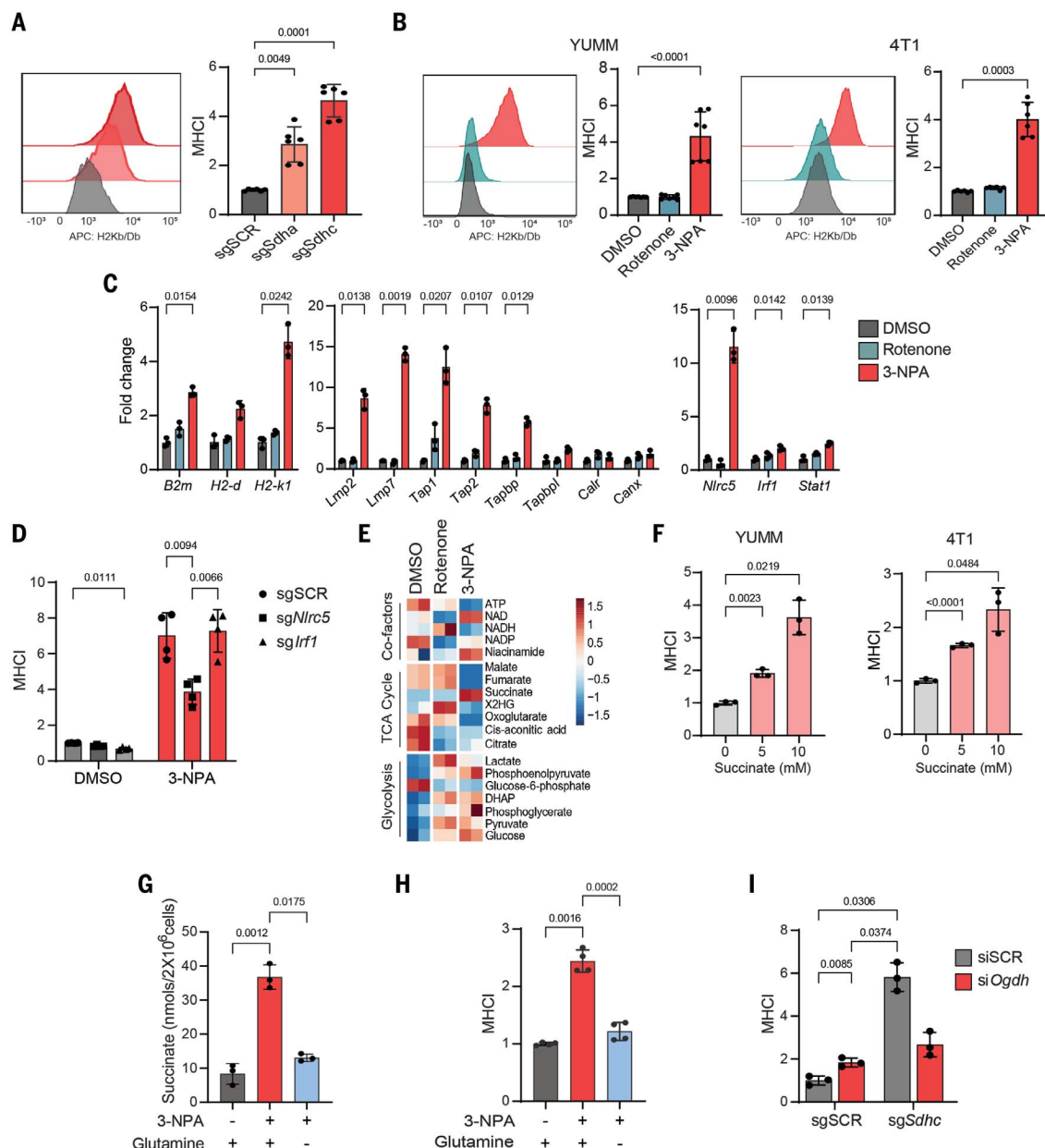


Fig. 2. Mitochondrial succinate drives MHC-I surface and gene expression upon inhibition of CIL. (A) Cell surface MHC-I expression on sgSCR, sgSdhA, and sgSdhC YUMML7 cells ($n = 6$). MHC-I expression is presented as fold change relative to sgSCR cells. A representative histogram is shown on the left. (B) Cell surface MHC-I expression on YUMML7 ($n = 6$) and 4T1 ($n = 6$) cells treated with DMSO (vehicle control), rotenone (CI inhibitor), or 3-NPA (CIL inhibitor) for 48 hours. MHC-I expression is presented as fold change relative to DMSO-treated cells. A representative histogram is shown on the left. (C) Reverse-transcription quantitative polymerase chain reaction (RT-qPCR) analysis of indicated representative MHC-APP genes in YUMML7 cells treated with DMSO, rotenone, and 3-NPA for 48 hours. Here, *B2m* is MHC-I light-chain; *H2-d* and *H2-k1* represent MHC-I heavy-chain; *Lmp2* and *Lmp7* represent immunoproteasome subunits; *Tap1*, *Tap2*, *Tapbp*, and *Tapbp1* represent antigen transporters and peptide loading complex in the endoplasmic reticulum; and *Nlrc5*, *Irf1*, and *Stat1* are transcription factors. Expression levels are presented as fold change relative to DMSO-treated cells. Each data point represents a technical replicate from one biological sample. Similar results were obtained with two independent biological replicates. (D) Cell surface MHC-I expression on DMSO- and 3-NPA-treated sgNlrc5 (NLRC5 knockout; $n = 4$) and sgIrf1 (IRF1 knockout; $n = 4$) YUMML7 cells. MHC-I expression is presented as fold change relative to DMSO-treated sgSCR (control) cells. (E) Steady-state levels of metabolites in

YUMML7 cells treated with DMSO, rotenone, and 3-NPA for 48 hours. A red-blue color scale depicts the abundance of the metabolites (red, high; blue, low) ($n = 2$ biologically independent experiments). (F) Cell surface MHC-I expression on YUMML7 ($n = 3$) and 4T1 ($n = 3$) cells treated with mono-methyl succinate (a cell-permeable form of succinate) dissolved in phosphate-buffered saline (PBS) for 48 hours. MHC-I expression is presented as fold change relative to vehicle (PBS) control cells. (G) Whole-cell succinate levels in YUMML7 cells cultured in the presence or absence of glutamine for 16 hours, followed by DMSO or 3-NPA treatment for 24 hours ($n = 3$). (H) Cell surface MHC-I expression on YUMML7 cells cultured in the presence or absence of glutamine for 16 hours followed by DMSO or 3-NPA treatment for 24 hours ($n = 4$). MHC-I expression is presented as fold change relative to DMSO-treated cells cultured in the presence of glutamine. (I) Cell surface MHC-I expression on sgSCR and sgSdhC (CIL knockout) YUMML7 cells transfected with either siSCR or siOgdh for 72 hours ($n = 3$). MHC-I expression is presented as fold change relative to cells transfected with siSCR (sgSCR). Data points in each panel represent an independent sample, unless otherwise specified. Data are plotted as means \pm SDs. Statistical significance was determined using one-way analysis of variance (ANOVA) with Dunnett's multiple comparisons test for (A), (B), (D), (F), (G), and (H); two-way ANOVA with Dunnett's multiple comparisons test for (C); and two-way ANOVA with Sidak's multiple comparisons test for (I).

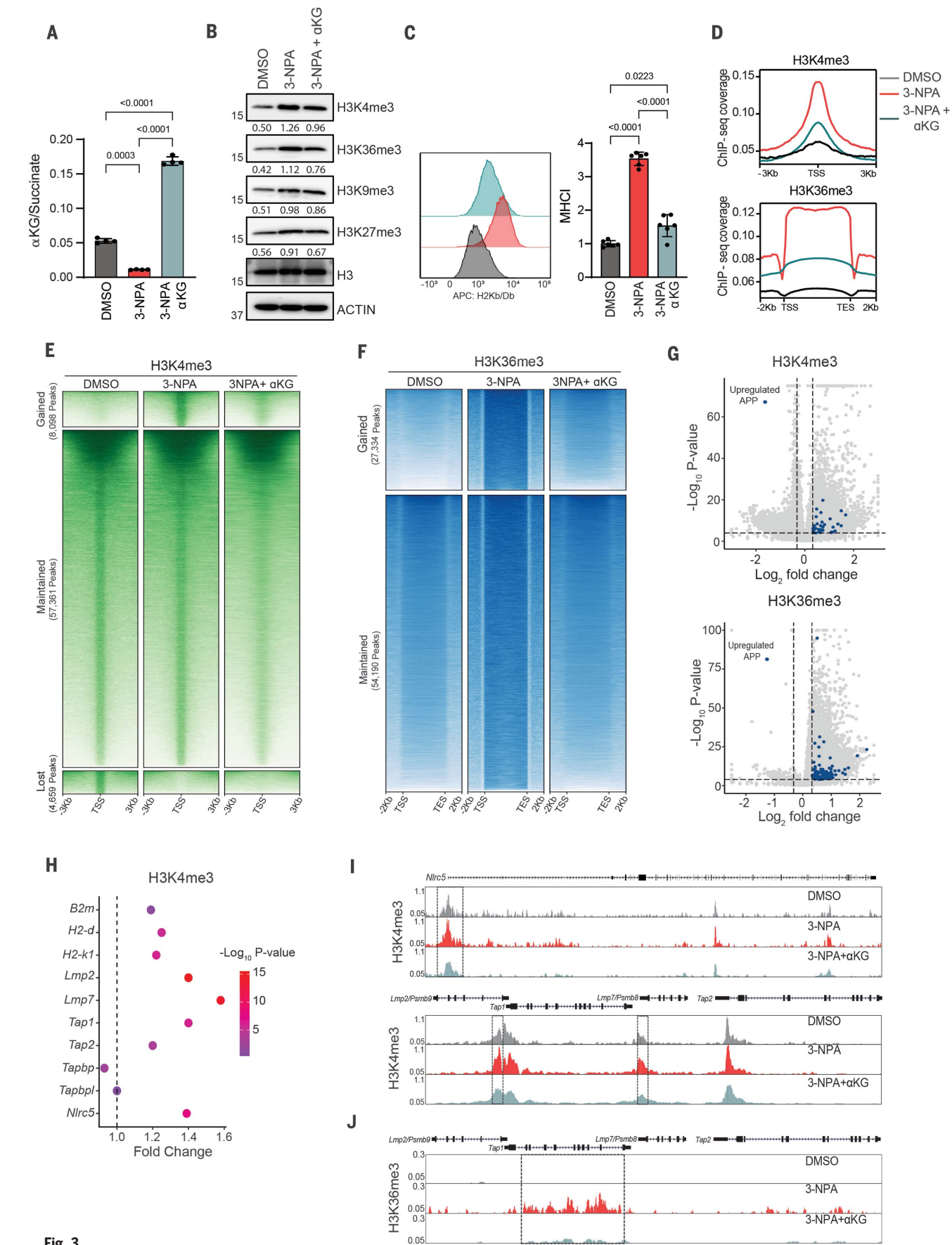


Fig. 3

Fig. 3. Mitochondrial succinate regulates antigen presentation through changes in histone methylation.

(A) The α KG/succinate ratio in YUMM1.7 cells treated with DMSO, 3-NPA, and 3-NPA + α KG for 6 hours ($n = 4$). (B) Immunoblot analysis of indicated lysine trimethylation marks on histone 3 in YUMM1.7 cells treated with DMSO, 3-NPA, and 3-NPA + α KG for 24 hours. Histone 3 and ACTIN are the loading controls. Numbers represents band density normalized to histone 3. Similar results were obtained with an independent experiment. (C) Cell surface MHC-I expression on YUMM1.7 cells treated with DMSO, 3-NPA, and 3-NPA + α KG for 48 hours ($n = 6$). MHC-I expression is presented as fold change relative to DMSO-treated cells. (D) Genome-wide distribution profiles of H3K4me3 (top) and H3K36me3 (bottom) binding based on ChIP-seq reads in YUMM1.7 cells treated with DMSO, 3-NPA, and 3-NPA + α KG for 24 hours. (E) Heatmap representation of H3K4me3 enrichment intensity based on ChIP-seq reads in YUMM1.7 cells treated with DMSO, 3-NPA, and 3-NPA + α KG for 24 hours. Signals within three kilobases of the transcription start site (TSS) are displayed in descending order for each cluster (i.e., gained, maintained, and lost in response to 3-NPA). (F) Heatmap representation of H3K36me3 enrichment intensity based on ChIP-seq reads in YUMM1.7 cells

treated with DMSO, 3-NPA, and 3-NPA + α KG for 24 hours. Signals within two kilobases around the gene body [TSS to TES (transcription end site)] are displayed in descending order for each cluster (i.e., gained and maintained in response to 3-NPA treatment). (G) Volcano plots showing differentially enriched genes for H3K4me3 (top) and H3K36me3 (bottom) modifications from ChIP-seq data comparing DMSO- and 3-NPA-treated YUMM1.7 cells ($P < 0.0001$ and fold change > 1.25). Peaks enriched for MHC-APP genes are depicted in blue. (H) Bubble plot showing fold change of H3K4me3 enrichment on promoters of representative MHC-APP genes from ChIP-seq dataset comparing DMSO- and 3-NPA-treated YUMM1.7 cells. Color gradient depicts the \log_{10} (P value). (I) Genome browser tracks for H3K4me3 marks at *Nlrp5*, *Psmb9*, *Tap1*, *Psmb8*, and *Tap2* loci in ChIP-seq. Boxes indicate significantly enriched peaks ($P < 0.0001$ and fold change > 1.25) at sites of interest. (J) Genome browser track for H3K36me3 at *Tap1* gene body in ChIP-seq. Box indicates significantly enriched peaks ($P < 0.0001$ and fold change > 1.25) at sites of interest. Data points in each panel represent an independent sample. Data are plotted as means \pm SDs. Statistical significance was determined by one-way ANOVA with Dunnett's multiple comparisons test for (A) and (C).

confirming enhanced APP upon CII inhibition (fig. S4E). To identify the molecular mechanism by which mitochondrial CII inhibition drives the expression of nuclear MHC-APP genes, we performed gene expression profiling on CII and CII inhibitor-treated YUMM1.7 cells (fig. S5A and tables S2, S3, and S4). CII-inhibited cells showed significant enrichment of the IFN response pathway, including APP genes (fig. S5A and tables S5 and S6). Therefore, we tested whether CII inhibition induces MHC-I through autocrine IFN-mediated signaling by knocking out *Ifngr1* or *Stat1* in YUMM1.7 cells (fig. S5B). Although IFN- γ -induced MHC-I up-regulation was eliminated in *Ifngr1* and *Stat1* knockout cells, CII inhibition still led to the induction of surface MHC-I and expression of APP genes in these cells (fig. S5, B to F). Similarly, CII inhibition did not induce signal transducers and activators of transcription 1 (STAT1) phosphorylation at Y701, which would be expected from receptor-mediated activation of IFN signaling (fig. S5G). Next, we tested whether CII inhibition-induced MHC-APP genes required NLR5 or IRF1—two known transcriptional activators of these genes. Notably, depletion of NLR5, but not of IRF1, attenuated CII inhibition-induced cell surface MHC-I and expression of MHC-APP genes (Fig. 2D and fig. S5, H and I). Together, these findings show that although IFN signaling is not required, there remains a partial dependence on NLR5-mediated transcription to induce MHC-APP genes in response to CII inhibition.

Because CII is succinate dehydrogenase and succinate influences nuclear gene expression (2), we investigated whether CII inhibition drives MHC-APP gene expression by promoting succinate accumulation. Four pieces of evidence indicate that this is the case. First, as predicted, CII-inhibited cells had high levels of succinate (Fig. 2E and fig. S6A). Second, treating wild-type (i.e., CII-competent) cells with cell-permeable succinate is sufficient to increase both cell surface MHC-I and expression of MHC-APP genes

(Fig. 2F and fig. S6, B to D). Third, because glutamine is the primary source of succinate in CII-inhibited cells (7), glutamine starvation of YUMM1.7 cells significantly reduced the 3-NPA-induced succinate accumulation and concomitant expression of cell surface MHC-I and MHC-APP genes (Fig. 2, G and H, and fig. S6E). Lastly, the knockdown of OGDH, a subunit of 2-oxoglutarate dehydrogenase, in CII knockout (*sgSdhc*) cells significantly reduced succinate levels and MHC-I expression (Fig. 2I and fig. S6, F to H). Consistent with this, an inverse correlation was identified between the expression of CII (especially *SDHC*) and MHC-APP encoding genes in the cancer cell line encyclopedia (CCLE) (fig. S7A). Furthermore, analysis of human breast and skin cancer samples from tumor sequencing studies identified significant down-regulation of MHC-APP genes in samples with high *SDHC* expression (fig. S7, B and C, and table S1). Therefore, CII inhibition elevates intracellular succinate that drives increased transcription of MHC-APP genes and antigen presentation in both mouse and human cancer cells. Many cancer cells escape the immune system by down-regulating MHC-APP expression or becoming unresponsive to the IFN- γ that activates these genes (25). Thus, our results that mitochondrial CII inhibition can up-regulate MHC-APP through succinate accumulation independently of IFN signaling have therapeutic implications.

Mitochondrial succinate increases MHC-APP gene transcription by inhibiting histone demethylases and modulating the tumor epigenetic landscape

Because intracellular α -ketoglutarate (α KG)/succinate ratio is an important determinant of the enzymatic activity of 2-oxoglutarate-dependent dioxygenases (2-OGDDs), including ten-eleven translocation (TET) family members and lysine-specific demethylases (KDMs) (2, 26, 27), we explored whether inhibition of CII decreases the α KG/succinate ratio, thereby

lowering 2-OGDD activity. Inhibition of CII or addition of cell-permeable succinate to YUMM1.7 cells significantly reduced the intracellular α KG/succinate ratio and increased trimethylation of several key lysine residues of histone H3 that are often associated with transcription regulation (fig. S8, A to D). Notably, cell-permeable α KG treatment of CII-inhibited (3-NPA) cells increased the α KG/succinate ratio and reversed H3 trimethylation, cell surface MHC-I, and expression of MHC-APP genes (Fig. 3, A to C, and fig. S8, E and F), consistent with succinate-mediated inhibition of 2-OGDDs being a key downstream effect of CII inhibition. Because treatment of CII-inhibited YUMM1.7 cells with 5-azacytidine (DNA methyltransferase inhibitor) did not prevent the increase in MHC-I expression but rather increased it further (fig. S8G), we conclude that inhibition of TET DNA demethylase activity by succinate is likely not a major contributor to CII inhibition-mediated MHC-APP expression.

The state of histone methylation is determined by the relative activities of KDMs and histone methyltransferases (fig. S9A). Succinate-mediated inhibition of KDMs shifts the balance toward increased histone methylation; therefore, we inhibited KDMs to determine whether they are involved in CII inhibition/succinate-mediated increases in MHC-APP. We found that inhibition of the KDM5 family (H3K4me3 demethylases) by KDM5-C70 increased MHC-I expression comparably to CII inhibition, accompanied by increased levels of H3K4me3 in YUMM1.7 cells (fig. S9, B and C). Next, we performed knockdown of the histone methyltransferases specific to H3K4me3 (KMT2A and KMT2B), H3K36me3 (SETD2), and H3K27me3 (EZH2) in CII knockout (*sgSdhc*) cells to restore the respective histone methylation (fig. S9D). Although knockdown of these did not affect the IFN- γ -induced increase in MHC-I, knockdown of KMT2A and SETD2 reversed the effects of increased succinate on expression of surface MHC-I and MHC-APP genes (fig. S9, E to H). Thus, H3K4me3 and H3K36me3

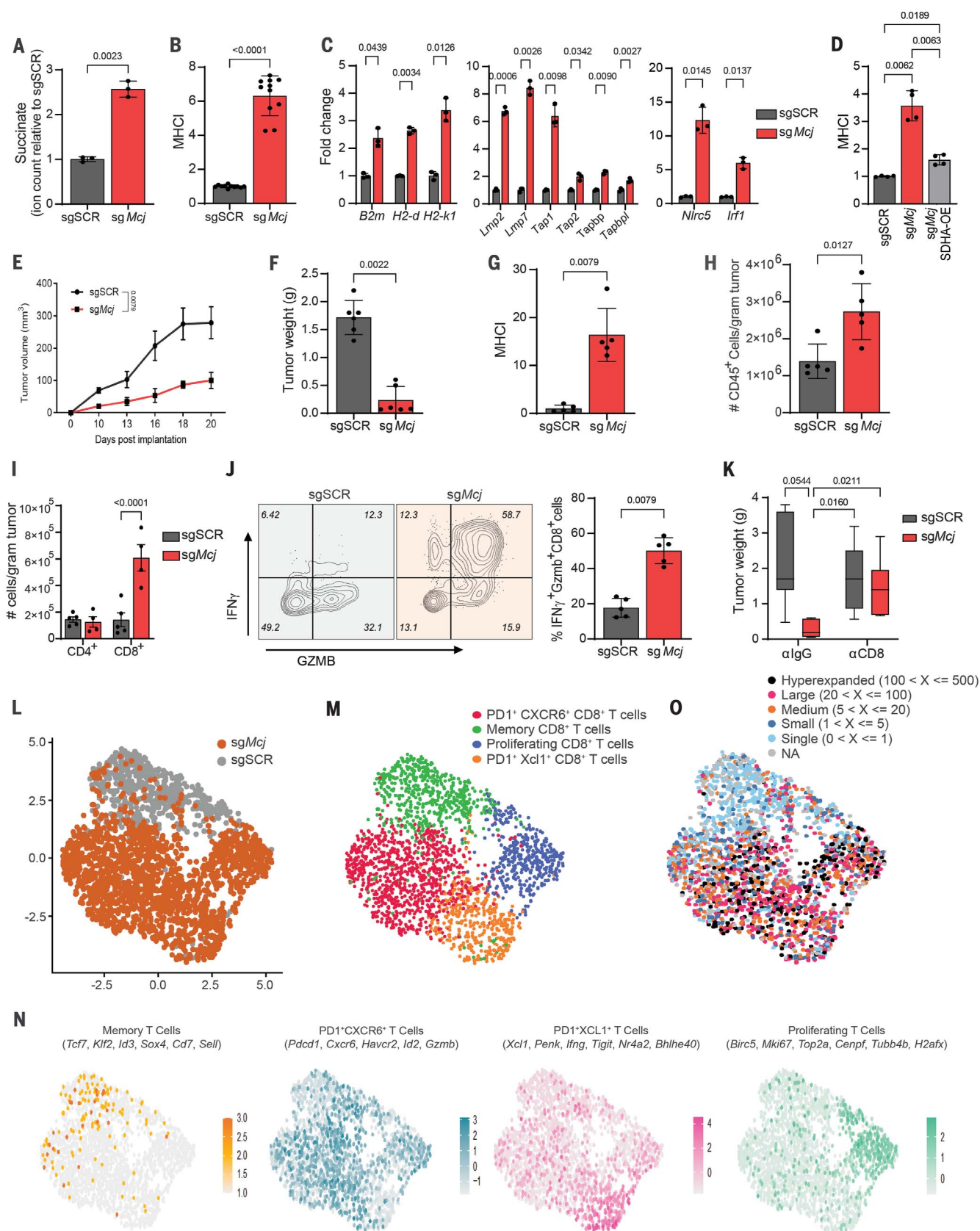


Fig. 4. Knockout of the mitochondrial CI inhibitor MCJ rewires the ETC to increase tumor immunogenicity without reducing OXPHOS: A therapeutic proof of concept. (A) Relative succinate levels in sgSCR (control) and sg *Mcj* (*Mcj* knockout) YUMM1.7 cells. Data are presented as fold change relative to sgSCR cells. (B) Cell

surface MHC-I expression on sgSCR and sg*Mcj* YUMM1.7 cells ($n = 10$). MHC-I expression is presented as fold change relative to sgSCR cells. (C) RT-qPCR analysis of indicated representative MHC-APP genes in sgSCR and sg*Mcj* YUMM1.7 cells. Expression levels are presented as fold change relative to sgSCR cells. Each data point represents a technical replicate of one biological sample. Similar results were obtained with an independent biological replicate. (D) Cell surface MHC-I expression on sg*Mcj* YUMM1.7 cells \pm SDHA overexpression ($n = 4$). Data are presented as the fold change relative to sgSCR-vector cells. (E to I) YUMM1.7-sgSCR ($n = 5$ mice) and sg*Mcj* ($n = 5$ mice) cells were subcutaneously injected in flanks of C57BL/6 male mice and monitored for tumor formation for 20 days. Shown are tumor growth curves (tumor volume versus time is plotted) (E), tumor weight at day 20 (in grams) (F), cell surface MHC-I expression relative to sgSCR tumor cells at day 20 (G), number of tumor-infiltrating CD45⁺ cells (per gram of tumor) at day 20 (H), and CD4⁺ and CD8⁺ T cells (per gram of tumor) at day 20 (I). These data are representative of three independent experiments. (J) Percentage of IFN- γ ⁺ and GZMB⁺ positive tumor infiltrating CD8⁺ T cells in sgSCR and sg*Mcj* YUMM1.7 tumors. (K) Tumor weights in grams of sgSCR and sg*Mcj* YUMM1.7 tumors from C57BL/6 mice treated with immunoglobulin G (IgG) isotype (α lgG) and anti-CD8 (α CD8) depleting antibodies for 21 days

every second day. (L) Uniform manifold approximation and projection (UMAP) of 8274 CD8⁺ T cells from YUMM1.7-sgSCR and sg*Mcj* tumors showing the formation of two clusters with the respective labels. Each dot corresponds to a single cell, color-coded by the sample type (gray, sgSCR; orange, sg*Mcj*). (M) UMAP from Seurat of CD8⁺ T cells into four distinct clusters according to differentiation and functional marker expression. Each dot represents a single cell, color-coded by the cluster type. (N) UMAPs showing average expression of functional signatures in CD8⁺ T cell clusters identified in (M). The differentiation and functional markers defining the cluster are shown at the top. (O) UMAP of CD8⁺ T cells overlaid with TCR clonal abundance. Each dot represents a single cell, color-coded by the number of TCR clones present. Data points in each panel represent an independent sample unless otherwise specified. Data are plotted as means \pm SDs for (A) to (D) and means \pm SEMs for (E) to (K). Statistical significance was determined by unpaired Welch t test for (A) and (B), two-way ANOVA with Dunnett's multiple comparisons test for (C), one-way ANOVA with Dunnett's multiple comparisons test for (D), unpaired Mann-Whitney test for (E) to (H) and (J), two-way ANOVA with Sidak's multiple comparisons test for (I), and two-way ANOVA with Tukey's multiple comparisons test for (K).

are key marks that regulate antigen presentation in response to succinate accumulation.

To assess the effect of CII inhibition on global epigenetic reprogramming, we performed chromatin immunoprecipitation sequencing (ChIP-seq) for H3K4me3 and H3K36me3 in YUMM1.7 cells treated with either 3-NPA, 3-NPA and α KG (to compete with succinate), or dimethyl sulfoxide (DMSO) as the vehicle control. As expected, H3K4me3 and H3K36me3 signals exhibited genome-wide gains after CII inhibition in YUMM1.7 cells, which were notably reversed by α KG supplementation (Fig. 3D and tables S7 to S10). Specifically, cells treated with 3-NPA showed an increase in 8098 peaks for H3K4me3 and 27,334 peaks for H3K36me3 compared with DMSO (Fig. 3, E and F). However, when α KG was added to the 3-NPA-treated cells, the global trends were reversed with only 2612 gained H3K4me3 peaks and 10,741 gained H3K36me3 peaks compared with DMSO (Fig. 3, E and F). Notably, several MHC-APP genes were significantly enriched for H3K4me3 and H3K36me3 (Fig. 3, G and H, and tables S11 and S12). For example, H3K4me3 levels were significantly increased in the promoter regions of *Nirc5*, *Psmb9*, *Tap1*, and *Psmb8*, and this was markedly reversed by α KG treatment (Fig. 3I). Similarly, the gene body of *Tap1* showed a marked increase in H3K36me3, which was significantly rescued by α KG treatment (Fig. 3J). On the basis of our transcription factor and epigenetic results, we propose a minimal model for how succinate activates MHC-APP transcription. That is, succinate accumulation downstream of CII inhibition alters the epigenetic landscape of the MHC-APP genes by suppressing KDM4 and KDM5 histone demethylase activity and increasing NLR5 levels that cooperatively induce transcription of the MHC-APP genes. This, in turn, promotes more-efficient tumor antigen presentation in YUMM1.7 melanoma cells. Although it is likely that other

transcription factors and epigenetic modifiers are involved in the effects of succinate that we observe, these results highlight that the MHC-I locus is responsive to even subtle epigenetic changes that might serve as a sensitive litmus test of mitochondrial ETC activity in cells.

Increasing relative electron flow through mitochondrial CI enhances tumor immunogenicity and T cell receptor (TCR) repertoire diversity

Previous studies have demonstrated the pro-inflammatory effects of succinate in macrophages and T cells (28–30). Our work also shows that accumulation of succinate within tumor cells is proinflammatory by increasing antigen presentation that activates T cell-mediated killing. However, systemic inhibition of CII is likely not a viable approach to increase tumor succinate levels because it could initiate de novo tumorigenesis, is neurotoxic, and very likely would have other adverse physiological effects in normal cells and tissues because of reduced mitochondrial ETC activity and adenosine 5'-triphosphate (ATP) production (28, 31). However, conditions that rewire the ETC in favor of CI-driven electron flow over that from CII might reduce CII activity enough to allow succinate accumulation without significant reductions in overall ETC activity and ATP production. The formation of CI-containing supercomplexes (e.g., the respirasome) has been proposed to generate two different pools of ubiquinone that enhance CI to CIII electron flow and concomitantly decrease the contribution from CII to CIII (32, 33). Methylation-controlled J protein (MCJ) is an endogenous CI-interacting protein in the inner mitochondrial membrane, knockout of which leads to increased CI activity over CII and the formation of supercomplexes (34). Thus, we hypothesized that rewiring the ETC by knockout of MCJ would reduce CII activity without reducing

overall ETC and ATP production and would provide increased succinate for MHC-APP expression and enhanced antitumor immunity. Notably, knockout of MCJ (*Mcj*-KO) in YUMM1.7 cells increased CI-containing supercomplexes and CI + CIII activity with an associated decrease in CII + CIII activity, resulting in increased levels of intracellular succinate, antigen presentation, and expression of MHC-APP genes (Fig. 4, A to C, and fig. S10, B and C). Similarly, YUMMER and B16-F10 *Mcj*-KO cells also had increased succinate and cell surface MHC-I and expression of MHC-APP genes (fig. S10, D to F). Notably, ectopic expression of SDHA or knockdown of *Ogdh* in *Mcj*-KO YUMM1.7 cells reduced MHC-I expression, demonstrating the importance of succinate in driving MHC-I expression (Fig. 4D and fig. S11, A to C). Furthermore, ChIP-quantitative polymerase chain reaction (qPCR) analysis of promoters of representative MHC-APP genes in *Mcj*-KO cells confirmed the increased H3K4me3 enrichment (fig. S11D), similar to direct CII inhibition. Next, we subcutaneously injected *Mcj*-KO YUMM1.7 cells into syngeneic C57BL/6 mice to test the effect of rewiring the ETC away from CII on tumor growth. Compared with control (sgSCR) YUMM1.7 tumors, *Mcj*-KO tumors grew substantially slower, maintained high levels of MHC-I, and contained greater numbers of CD45⁺ immune cells, especially CD8⁺ T cells (Fig. 4, E to I, and fig. S12A), thus mirroring the effects that we observed in CII knockout YUMM1.7 cells in vivo. Similar results were observed in the more immunogenic YUMMER mouse melanoma tumor model (35) (fig. S12, B to D). Further inspection of tumor-infiltrating CD8⁺ T cells showed that the cells from sgSCR control tumors expressed activation markers CD44 and CD69 as well as the TCF-1 transcription factor (which is important for memory T cells and their precursors, encoded

by the *Tcf7* gene), whereas CD8⁺ T cells in *Mcj*-KO tumors expressed greater amounts of PD-1, TIM3, CXCR6, TOX, and effector molecules such as IFN- γ and GZMB (Fig. 4J and fig. S12E). Furthermore, antibody-mediated depletion of CD8⁺ T cells restored the growth of *Mcj*-KO tumors, confirming the role of CD8⁺ T cells in tumor control (Fig. 4K). These results show that the CD8⁺ tumor-infiltrating lymphocytes (TILs) in the *Mcj*-KO tumors receive more antigenic signaling compared with control (sgSCR) tumors, which induces their differentiation into effector and exhausted cell states.

Next, we performed single-cell transcriptomics coupled with single-cell TCR sequencing to profile the mRNA and TCR $\alpha\beta$ repertoire of CD8⁺ T cells from YUMM1.7 *Mcj*-KO and sgSCR tumors. Notably, cells from *Mcj*-KO and sgSCR tumors clustered distinctively (Fig. 4L and fig. S13A). Although the majority of the CD8⁺ T cells in sgSCR tumors clustered together and displayed signatures of memory CD8⁺ T cells (*Tcf7*, *Klf2*, *Id3*, *Sox4*, *Sell*, *Cxcr3*, *Gzma*, *Gzmk*, *Cd69*, and *Il7r*), the CD8⁺ T cells from *Mcj*-KO tumors clustered into PDI⁺ CXCR6⁺ CD8⁺ T cells (*Pdcd1*, *Cxcr6*, *Havcr2*, *Id2*, *Gzmb*, *Cd38*, and *Fasb*), PDI⁺ XCL1⁺ CD8⁺ T cells (*Xcl1*, *Penk*, *IFN γ* , *Tigit*, *Nr4a2*, *Bhlhe40*, *Csf2*, *Ccl*, and *Prfl*), and proliferating PDI⁺ CD8⁺ T cells (*Birc5*, *Mki67*, *Top2a*, *Cenpf*, *Tubb4b*, *H2afx*, *Pdcd1*), confirming observations from fluorescence-activated cell sorting (FACS) analysis (Fig. 4, M and N). Additionally, although most CD8⁺ T cells from sgSCR controls had unique, single TCR clonotypes (clone size of 1) with high clonotype diversity as calculated by the Shannon, Chao, and ACE indexes (fig. S13, B and C), CD8⁺ T cells from *Mcj*-KO consisted of hyperexpanded clones (>100 T cells with identical TCR α and β -chain) that expressed *Pdcd1*, *Cxcr6*, *Gzmb*, and *IFN γ* genes (within the top 10 abundant clones) (Fig. 4O and fig. S13, D and E). Notably, although only a few clones were present in both sgSCR and *Mcj*-KO tumors, most of the expanded clones in *Mcj*-KO tumors were unique (fig. S13F), which points to increased expression of a broader set of tumor antigens as a result of increased MHC-I. Collectively, these results show that increasing intracellular tumor succinate and MHC-I (through *Mcj*-KO or direct CII inhibition) potentiates tumor cell immunogenicity and the activation and infiltration of more tumor-reactive effector CD8⁺ T cells that suppress tumor growth. Our results indicate that discrete rewiring of the ETC to moderately reduce CII activity or increase succinate in tumors not only improves T cell engagement by increasing MHC-I but also enhances the selective expansion of protective T cell clones, which suggests that tumor

MHC-I levels determine tolerogenic versus immunogenic set points for tumor antigens. Thus, this ETC-rewiring approach might represent a one-two punch to convert cold tumors to hot and to improve antitumor responses and immunotherapy efficacy.

REFERENCES AND NOTES

- R. J. DeBerardinis, N. S. Chandel, *Sci. Adv.* **2**, e1600200 (2016).
- I. Martínez-Reyes, N. S. Chandel, *Nat. Commun.* **11**, 102 (2020).
- I. Martínez-Reyes et al., *Nature* **585**, 288–292 (2020).
- L. F. Dong et al., *eLife* **6**, e22187 (2017).
- A. S. Tan et al., *Cell Metab.* **21**, 81–94 (2015).
- M. Kim, M. Mahmood, E. Reznik, P. A. Gammage, *Trends Cancer* **8**, 1046–1059 (2022).
- C. Lussey-Lepoutre et al., *Nat. Commun.* **6**, 8784 (2015).
- R. K. Aggarwal et al., *Proc. Natl. Acad. Sci. U.S.A.* **118**, e2106947118 (2021).
- R. K. Gopal et al., *Proc. Natl. Acad. Sci. U.S.A.* **115**, E6283–E6290 (2018).
- D. Lorendeau et al., *Metab. Eng.* **43**, 187–197 (2017).
- A. N. Gorelick et al., *Nat. Metab.* **3**, 558–570 (2021).
- M. L. Hart et al., *eLife* **12**, e78654 (2023).
- K. Birsoy et al., *Cell* **162**, 540–551 (2015).
- K. Meeth, J. X. Wang, G. Micevic, W. Damsky, M. W. Bosenberg, *Pigment Cell Melanoma Res.* **29**, 590–597 (2016).
- J. MacFarlane et al., *Clin. Endocrinol.* **93**, 528–538 (2020).
- M. P. Murphy, E. T. Chouchani, *Nat. Chem. Biol.* **18**, 461–469 (2022).
- F. Al Khazal et al., *FASEB J.* **35**, e21227 (2021).
- N. Armstrong et al., *Cell Rep.* **38**, 110453 (2022).
- J. P. Bayley et al., *PLOS ONE* **4**, e7987 (2009).
- C. Lepoutre-Lussey et al., *Mol. Cell. Endocrinol.* **421**, 40–48 (2016).
- J. I. Piruat, C. O. Pintado, P. Ortega-Sáenz, M. Roche, J. López-Barneo, *Mol. Cell. Biol.* **24**, 10933–10940 (2004).
- H. Dannenberg et al., *Am. J. Pathol.* **157**, 353–359 (2000).
- E. Edström et al., *Am. J. Pathol.* **156**, 651–659 (2000).
- L. Fishbein et al., *Cancer Cell* **31**, 181–193 (2017).
- K. Dhatchinamoorthy, J. D. Colbert, K. L. Rock, *Front. Immunol.* **12**, 636568 (2021).
- J. A. Losman, P. Koivunen, W. G. Kaelin Jr., *Nat. Rev. Cancer* **20**, 710–726 (2020).
- M. Xiao et al., *Genes Dev.* **26**, 1326–1338 (2012).
- X. Chen et al., *Sci. Immunol.* **7**, eabm8161 (2022).
- I. Elia et al., *Cell Metab.* **34**, 1137–1150.e6 (2022).
- G. M. Tannahill et al., *Nature* **496**, 238–242 (2013).
- A. C. Ludolph, F. He, P. S. Spencer, J. Hammerstad, M. Sabri, *Can. J. Neurol.* **18**, 492–498 (1991).
- E. Calvo et al., *Sci. Adv.* **6**, eaba7509 (2020).
- E. Lapuente-Brun et al., *Science* **340**, 1567–1570 (2013).
- K. M. Hatle et al., *Mol. Cell. Biol.* **33**, 2302–2314 (2013).
- J. Wang et al., *Pigment Cell Melanoma Res.* **30**, 428–435 (2017).
- G. Mendiratta, G. Mendiratta/Complex2-RNAseq: Complex2-RNAseq code, Zenodo (2023); <https://doi.org/10.5281/zenodo.8191267>.

ACKNOWLEDGMENTS

We thank members of the Shadel, Kaech, and Hargreaves laboratories for helpful scientific discussions, reagents, and experimental support; K. Miller and V. Tripple for laboratory management and moral support; E. Stites for critical reading of the initial draft of the manuscript; Q. Yan and X. Cheng for helpful scientific insight and discussions; C. O'Connor and the staff at the Salk Flow Cytometry Core Facility (funded by NIH-NCI CCSG P30 014195 and shared instrumentation grant S10-OD023689); C. Fine and V. Nguyen at the UCSD/Sanford Consortium Human Embryonic Stem Cell Core for cell sorting and FACS analysis; the Salk Waitt Advanced Biophotonics Core Facility (funding by NIH-NCI CCSG P30 014195 and the Waitt Foundation); Y. Hang from the Salk Razavi Newman Integrative Genomics and Bioinformatics Core Facility (funding by NIH-NCI CCSG P30 014195 and the Helmsley Trust); and the Salk NGS Core Facility (funded by NIH-NCI CCSG P30 014195, the Chapman Foundation, and the Helmsley Charitable Trust). Schematics were generated using BioRender (<https://www.biorender.com/>). **Funding:** This study was

supported by NIH grants R01 CA216101 to G.S.S. and S.M.K., R01 CA228211 to G.S.S. and D.C.H., R35CA242379 to M.G.V.H., and R21 AI151562 to S.M.K. K.C.M. and D.C. were each supported by a Salkexcellerators postdoctoral fellowship. S.K.V. was supported by CRI and a National Cancer Center postdoctoral fellowship. S.K.V. and D.C. were each supported by a NOMIS Center postdoctoral fellowship. K.L.A. was supported by the National Science Foundation (DGE-1122374) and NIH grants (F31CA271787 and T32GM007287). A.G.S. was supported by an NIA grant (F31AG062099). P.B.E.M. was supported by a research fellowship from Fundación Alfonso Martín Escudero (Spain). N.T. was supported by a postdoctoral fellowship from the Salk Paul F. Glenn Center for Biology of Aging Research. G.M. was supported by the Conrad Prebys Foundation. G.S.S. holds the Audrey Geisel endowed Chair of Biomedical Science, S.M.K. holds the NOMIS endowed chair, and D.C.H. holds the Richard A. Heyman and Anne E. Diagle Endowed Developmental Chair. G.S.S. and the Salk core facilities are also supported by the San Diego Nathan Shock Center, NIH P30AG068635. **Author contributions:** G.S.S. and S.M.K. were responsible for overall project management and funding and the conceptualization of the project. K.C.M., S.K.V., G.S.S., and S.M.K. designed experiments. K.C.M., S.K.V., M.A.J., M.J.B., G.R.R., P.B.E.M., A.G.S., N.T., and Y.F. performed experimental work and analyzed the data. G.M. performed CCLE and human tumor data analysis. K.L.A., T.K., and M.G.V.H. performed metabolomics and analyzed data. D.C. helped with single-cell RNA sequencing (scRNA-seq) and animal work. B.P. and F.A.H. helped with animal experiments. M.R. and M.B. provided cell lines and materials. M.R., M.B., and D.C.H. provided input on study design, data analysis, and interpretation. K.C.M., S.K.V., S.M.K., and G.S.S. wrote the manuscript. **Competing interests:** G.S.S. is on the scientific advisory board and has equity in Mitotherapeutics. S.M.K. is on the scientific advisory boards and has equity in EvolveImmune Therapeutics, Simcha Therapeutics, Affini-T Therapeutics, Arvinas, and Pfizer. M.G.V.H. is on the scientific advisory board in Agios Pharmaceuticals, iTeos Therapeutics, Sage Therapeutics, Pretzel Therapeutics, Lime Therapeutics, Doria Ventures, and Auron Therapeutics. M.R. is a cofounder and member of the scientific advisory board of Mitotherapeutics, LLC. M.B. receives funding for unrelated research activities from AstraZeneca. M.R. is an inventor on the patent applications 14/413,927 and 15/805,534 submitted by the University of Vermont that cover the use of method and compositions for metabolic regulation. M.R. is an inventor on the patent application 15/551,995 submitted by the University of Vermont that covers the use of MCJ agonists and uses thereof. M.R. is an inventor on the patent application 15/743,096 submitted by the University of Vermont that covers the use of method and compositions to treat drug-induced diseases and conditions. M.R. is an inventor on the patent application 62/979,833 submitted by the University of Vermont and Mitotherapeutics that covers the use of compositions and methods for inhibiting expression of MCJ. The remaining authors declare no competing interests. **Data and materials availability:** Sequencing data (bulk RNA-seq, scRNA-seq, and ChIP-seq) generated in this study are available at the Gene Expression Omnibus (GEO) under accession codes GSE198348 and GSE235311. CCLE RNA-seq data can be found through the link <https://sites.broadinstitute.org/ccle>. Codes used to analyze the human tumor RNA-seq data are deposited to Zenodo (36). All the data are available in the main text or the supplementary materials. Other materials generated in this manuscript are available from the corresponding authors upon reasonable request and, when applicable, fulfillment of appropriate material transfer agreements. **License information:** Copyright © 2023 the authors, some rights reserved; exclusive licensee American Association for the Advancement of Science. No claim to original US government works. <https://www.science.org/about/science-licenses-journal-article-reuse>

SUPPLEMENTARY MATERIALS

science.org/doi/10.1126/science.abq1053
Materials and Methods
Figs. S1 to S14
Tables S1 to S17
References (37–48)
MDAR Reproducibility Checklist

Submitted 22 March 2022; resubmitted 21 June 2023
Accepted 2 August 2023
10.1126/science.abq1053